



PAPER

Differentiation between strain and charge mediated magnetoelectric coupling in $\text{La}_{0.7}\text{Sr}_{0.3}\text{MnO}_3/\text{Pb}(\text{Mg}_{1/3}\text{Nb}_{2/3})_{0.7}\text{Ti}_{0.3}\text{O}_3(001)$

OPEN ACCESS

RECEIVED
9 February 2021REVISED
26 April 2021ACCEPTED FOR PUBLICATION
25 May 2021PUBLISHED
17 June 2021

Original content from
this work may be used
under the terms of the
[Creative Commons
Attribution 4.0 licence](#).

Any further distribution
of this work must
maintain attribution to
the author(s) and the
title of the work, journal
citation and DOI.



T Bhatnagar-Schöffmann^{1,2,3,*} , E Kentzinger^{1,*} , A Sarkar¹ , P Schöffmann^{1,3} ,
Q Lan² , L Jin^{1,2} , A Kovács² , A J Grutter⁴ , B J Kirby⁴ , R Beerwerth⁵ ,
M Waschk¹, A Stellhorn^{1,3} , U Rücker¹ , R E Dunin-Borkowski² and
Th Brückel^{1,3}

¹ Forschungszentrum Jülich GmbH, Jülich Centre for Neutron Science (JCNS-2) and Peter Grünberg Institut (PGI-4), JARA-FIT, 52425 Jülich, Germany

² Forschungszentrum Jülich GmbH, Ernst Ruska-Centre for Microscopy and Spectroscopy with Electrons and Peter Grünberg Institute (PGI-5), 52425 Jülich, Germany

³ RWTH Aachen, Lehrstuhl für Experimentalphysik IVc, Jülich-Aachen Research Alliance, JARA-FIT, 52074, Aachen, Germany

⁴ NIST Center for Neutron Research, NIST, Gaithersburg, MD, United States of America

⁵ Forschungszentrum Jülich GmbH, Jülich Centre for Neutron Science at MLZ, Lichtenbergstrasse 1,85748, Garching, Germany

* Authors to whom any correspondence should be addressed.

E-mail: t.bhatnagar-schoeffmann@fz-juelich.de and e.kentzinger@fz-juelich.de

Keywords: magnetoelectric, magnetism, polarized neutron reflectometry, transmission electron microscopy, thin films

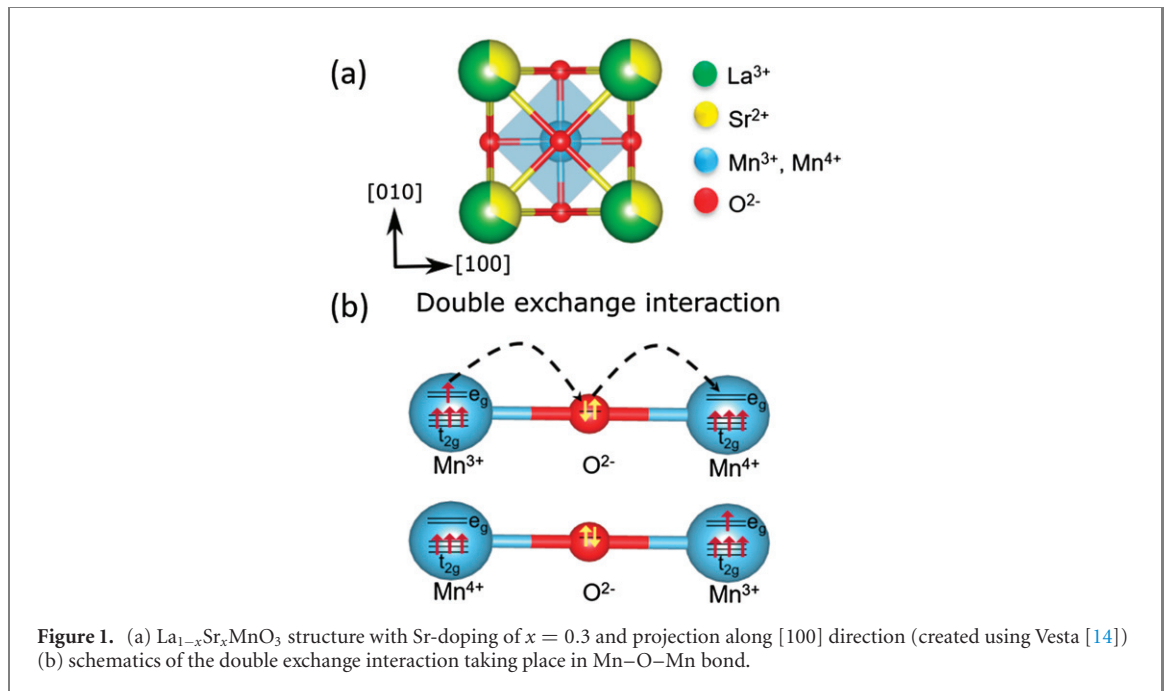
Supplementary material for this article is available [online](#)

Abstract

Magnetoelectric (ME) coupling in $\text{La}_{0.7}\text{Sr}_{0.3}\text{MnO}_3/\text{Pb}(\text{Mg}_{1/3}\text{Nb}_{2/3})_{0.7}\text{Ti}_{0.3}\text{O}_3$ (LSMO/PMN–PT (001)) has been probed in the past years to identify the underlying mechanism behind it. PMN–PT, which is well known for its excellent piezoelectric properties, also exhibits ferroelectricity. This motivates our interest to differentiate which effect is dominant for this ‘voltage control of magnetism’. Here, we present results for the ME coupling at different temperatures: 300 K and 80 K. In this article we discuss and explain, how the nature of ME coupling is influenced by different parameters such as magnetic field, electric field, directional dependence (hard axis, easy axis) and temperature. Owing to large lattice mismatch between LSMO and PMN–PT, the strain-mediated coupling is strongly prevalent, however the change in strain behaviour from butterfly loop to linear loop is observed as a function of temperature. ME measurements are performed along hard axis [100] and easy axis [110] of LSMO in the presence of remanent magnetic field which showcases the pure influence of electric field on the system, resulting in a combination of strain- and charge-mediated coupling. The magnetic depth profile is probed by polarized neutron reflectometry as a function of electric field which demonstrates the existence of an interlayer with reduced nuclear scattering length density and reduced magnetic scattering length density at the interface. From transmission electron microscopy, stoichiometric variations are observed due to the presence of Mn_3O_4 particles at the interface.

1. Introduction

Magnetoelectric (ME) coupling is an interesting phenomenon enabling the direct control of magnetization via electric field, or vice-versa. It was first mentioned in Maxwell’s equation that magnetic interaction and electric charge motion are intrinsically coupled, thereby opening up the playground for ‘voltage control of magnetism (VCM)’. With the increasing demand for low power consumption in magnetic storage devices, it has become critical to look for systems where magnetization can be manipulated by an applied electric field. Non-volatile and energy efficient spintronic logic devices are proposed which are based



on ME coupling [1]. Such devices pose as potential candidates for advanced CMOS technology. Different approaches have been employed to investigate this effect which can be achieved by various mechanisms, namely: strain mediation [2], carrier modulation [3], exchange coupling [4] and orbital reconstruction [5]. With these mechanisms at play, researchers started to develop artificial multiferroic heterostructures by coupling magnetic and ferroelectric materials like Fe/BaTiO₃ [2], $\text{La}_{0.67}\text{Sr}_{0.33}\text{MnO}_3/\text{BaTiO}_3$ [6] CoFe/BiFeO₃ [7], $\text{PbZr}_{0.2}\text{Ti}_{0.8}\text{O}_3/\text{La}_{0.8}\text{Sr}_{0.2}\text{MnO}_3$ [8] and $\text{La}_{0.7}\text{Sr}_{0.3}\text{MnO}_3/\text{Pb}(\text{Mg}_{1/3}\text{Nb}_{2/3})_{0.72}\text{Ti}_{0.28}\text{O}_3$ [9]. In the past, Thiele *et al* [9] reported strain-mediated ME coupling in the $\text{La}_{0.7}\text{Sr}_{0.3}\text{MnO}_3/\text{Pb}(\text{Mg}_{1/3}\text{Nb}_{2/3})_{0.72}\text{Ti}_{0.28}\text{O}_3$ (001) system and recently, Pati and Taniyama [10] observed coexistence of volatile and non-volatile ME behaviour in this system. With the lattice mismatch of +3.5% between LSMO and PMN–PT, the strain engineering becomes an interesting tool to control the functionality.

In this article, we report on the voltage induced effects in a ferromagnetic and ferroelectric/piezoelectric thin film heterostructure system: $\text{La}_{0.7}\text{Sr}_{0.3}\text{MnO}_3$ (LSMO) on single crystalline $\text{Pb}(\text{Mg}_{1/3}\text{Nb}_{2/3})_{0.7}\text{Ti}_{0.3}\text{O}_3$ [PMN–0.3PT(001)] grown using molecular beam epitaxy (MBE) in oxygen atmosphere. LSMO, a complex magnetic oxide possesses strong couplings between lattice, charge, spin and orbital degrees of freedom [11] and exhibits a series of magnetic phases depending on the Sr doping. Here, we use a Sr-doping of $x = 0.3$ ($\text{La}_{1-x}\text{Sr}_x\text{MnO}_3$) which leads to semi-metallic ferromagnetic LSMO [12]. With Sr-doping, holes are generated at the Mn site leading to $(1-x)\text{Mn}^{3+}(3d^4)$ and $(x)\text{Mn}^{4+}(3d^3)$ valencies of Mn-ions. Due to the presence of mixed valence states of Mn-ions, double exchange interaction takes place as shown in figure 1 favouring strong ferromagnetic ordering [13].

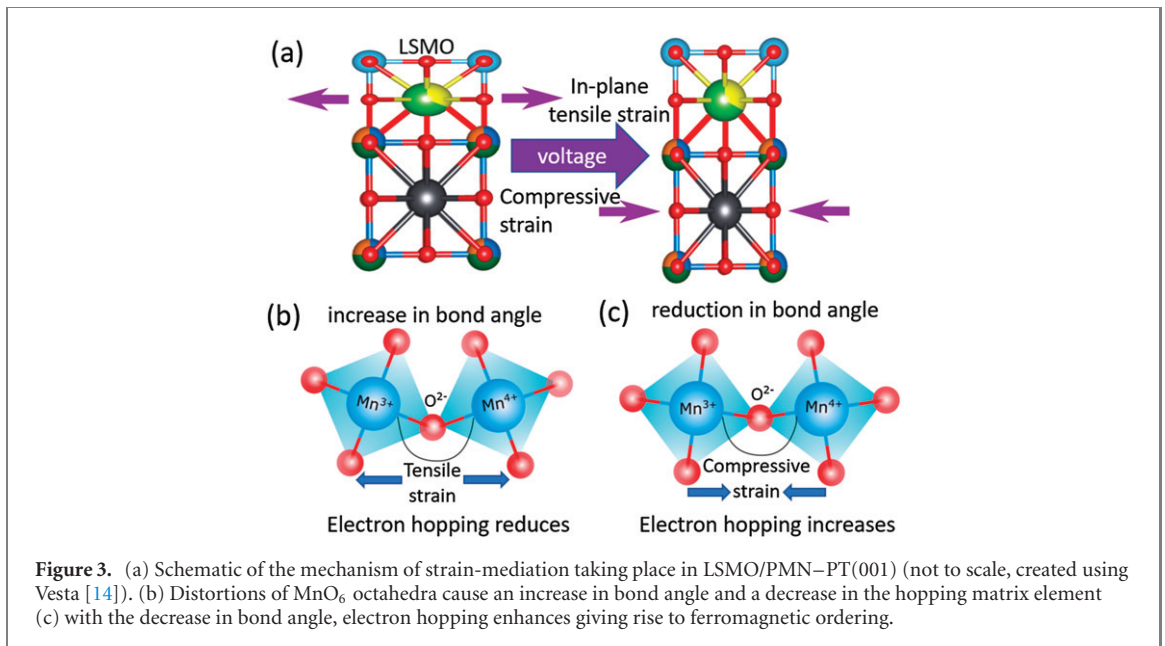
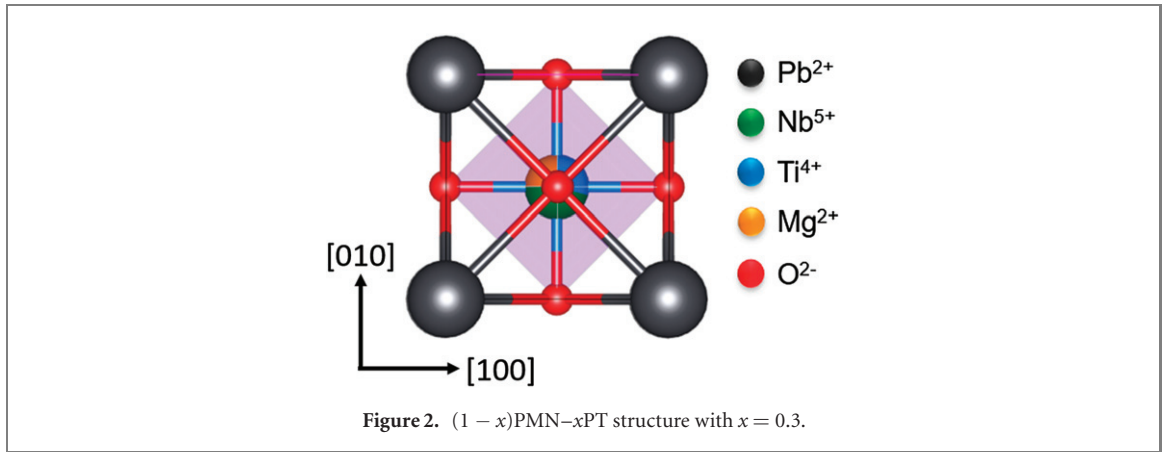
On the other hand, single crystal PMN–0.3PT(001) is a relaxor ferroelectric oxide and exhibits excellent piezoelectricity. Relaxor ferroelectrics are disordered ferroelectrics comprising of randomly distributed polar nano-regions with different directions of electric dipole moments. On applying a high electric field, these nano-domains orient themselves with the field resulting in a large polarization. However, on removing the electric field, most of these nano-domains re-acquire their random orientation causing a slimming down of the hysteresis loop compared to classical ferroelectric like BaTiO₃ [15].

PMN–0.3PT(001) has a pseudo-cubic structure with a lattice constant of $a = 4.02 \text{ \AA}$ and $\alpha = \beta = \gamma = 89.90^\circ$, see figure 2. It can have eight possible polarization directions along $\langle 111 \rangle$ and three types of domain switching: 71° , 109° (ferroelastic) and 180° (ferroelectric). The total polarization in PMN–PT is calculated by adding the two phases PMN and PT [16]. PMN is responsible for the formation of polar nano regions due to off-central displacement of Mg^{2+} and Nb^{5+} cations in the octahedral sites of the perovskite, whereas PbTiO_3 accounts for polarization arising from off-central displacement of Ti^{4+} cation in the oxygen octahedral cage:

$$P_r^{\text{total}} = P_r^{\text{Ti}} x^{\text{PT}} + P_r^{\text{PMN}} x^{\text{PMN}}, \quad (1)$$

where P_r^{Ti} and P_r^{PMN} are polarization values of PT and PMN phases with their corresponding concentrations.

The proposed mechanism of strain-mediation occurring in LSMO/PMN–PT(001) is explained by figure 3(a). When LSMO is deposited on PMN–PT, it experiences an in-plane tensile strain due to the



lattice mismatch, causing distortions of MnO_6 octahedra [17, 18] and thereby increasing the Mn–O–Mn bond angle as shown in figure 3(b). This leads to a reduction of the electron hopping matrix element and hence, destabilizes the ferromagnetism. On applying the voltage across the structure, PMN-PT experiences in-plane compressive strain, which is transferred to LSMO. As a result, the Mn–O–Mn bond angle reduces (figure 3(c)), going towards 180° , thereby increasing the electron hopping matrix element and thus, stabilizing the ferromagnetism.

To verify and identify the ME coupling mechanism taking place in LSMO/PMN-PT(001), we have applied a combination of microscopic and macroscopic techniques, and achieved a comprehensive view of the voltage induced effects occurring in LSMO/PMN-PT(001). We find that ME coupling in this system has strong temperature and directional dependence. We argue that this dependence is related to different mechanisms playing a role along different directions of LSMO (hard and easy axes) and temperatures. In addition, change in coercive field (H_C) is observed, along with presence of negative remanence at room temperature. We are able to disentangle these effects by a combination of several experimental techniques.

2. Experimental

$\text{La}_{0.7}\text{Sr}_{0.3}\text{MnO}_3$ thin films of 320 Å nominal thickness are deposited on (001)-oriented PMN-PT single crystal substrates using an MBE system with a base pressure of 2×10^{-8} Pa. The substrates are pre-annealed at 730°C for 1 h in oxygen atmosphere. The growth rates of the individual elements, La, Sr and Mn, are calibrated in oxygen atmosphere using a quartz micro balance mounted at the substrate position. An oxygen plasma source is used to provide atomic oxygen. The thin films of LSMO are co-deposited on to the PMN-PT(001) substrate at 730°C under a pressure of 5.8×10^{-4} Pa with an oxygen flow of 0.15 sccm.

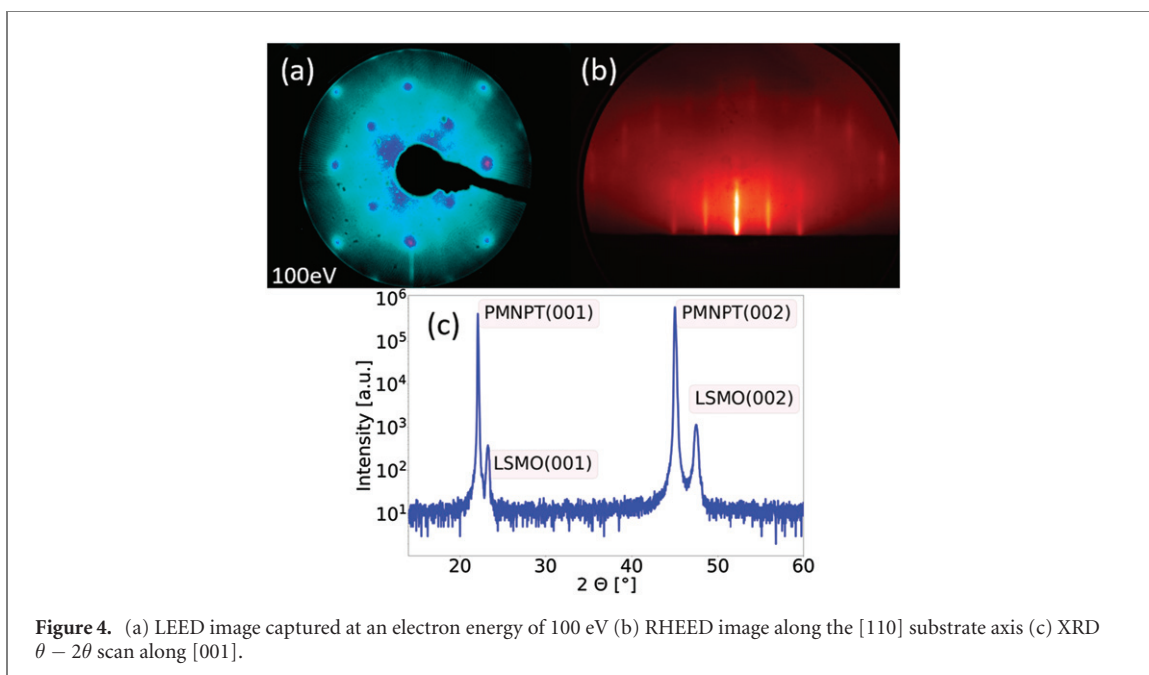


Figure 4. (a) LEED image captured at an electron energy of 100 eV (b) RHEED image along the [110] substrate axis (c) XRD $\theta - 2\theta$ scan along [001].

After that, the sample is post-annealed at 200 °C for 30 min and then cooled to room temperature in the same atmosphere. The growth optimization for depositing $\text{La}_{0.7}\text{Sr}_{0.3}\text{MnO}_3$ are adapted from elsewhere [19].

SQUID—magnetometry measurements are performed to study the ME properties of LSMO/PMN–PT(001). The magnetic depth profile as a function of voltage is investigated with polarized neutron reflectometry (PNR). These PNR measurements are performed using the polarized beam reflectometer at NCNR, NIST. The sample is structurally characterized *in situ* using low energy electron diffraction (LEED), reflection high energy electron diffraction (RHEED) and *ex situ* by x-ray diffraction (XRD) with a diffractometer using a CuK_α source ($\lambda = 1.5406 \text{ \AA}$). Transmission electron microscopy (TEM) and energy-dispersive x-ray spectroscopy measurements in scanning mode were carried out using a spherical aberration corrected TEM operated at 200 kV [20] and the sample is prepared by cutting a thin cross-section lamella using focussed ion beam milling. A 500 Å Au layer is deposited via sputtering to prevent charging during the ion milling process.

3. Results and discussion

3.1. Structural characterizations

The sample is structurally characterized *in situ* by LEED and RHEED figures 4 (a) and (b). Both techniques are surface sensitive and confirm the presence of a smooth surface of the film and the absence of any surface reconstruction. The XRD measurement in figure 4(c) shows the growth of LSMO in (001)-orientation. Only film and substrate peaks are visible.

The calculated out-of-plane lattice constant, c , for LSMO is found to be $c_{\text{LSMO}} = 3.82 \text{ \AA}$ which is 1.3% lower than the bulk value, $c_{\text{bulk}} = 3.87 \text{ \AA}$. Taking the in-plane lattice mismatch of +3.5% between PMN–PT(001) and LSMO into account, the reduction rate of 1.3% in the out-of-plane lattice constant indicates that the strain in LSMO is partially relaxed. From the high-angle annular dark field scanning transmission electron microscopy (HAADF-STEM) image figure 5(a) one can clearly see the epitaxial and strained growth of LSMO on PMN–PT(001). Figure 5(b) shows that, as the thickness increases above $\sim 30\text{--}40 \text{ \AA}$, the film starts relaxing partially by forming defects depicted in figure 5(c). The yellow structure represents the formation of dislocation [21] where the local distortion resulting from the insertion of an extra half atomic plane is evident. The bulk of the film retains an in-plane tensile strain of 0.7%. The thickness of the film was determined by x-ray reflectometry to be $326 \pm 3 \text{ \AA}$.

3.2. ME measurements

The ME properties are measured by MPMS-SQUID with a special set-up adapted from Borisov *et al* [22]. We have used such a set-up in the study of ME coupling in LSMO/BTO heterostructures [6] and VCM of magnetic nanoparticles on ferroelectric substrates [23, 24]. For a uniform application of voltage, an Au layer is deposited as a bottom electrode and LSMO serves as a top electrode. The ME behaviour is studied as a function of temperature with magnetic field and in remanent magnetic field. When LSMO experiences

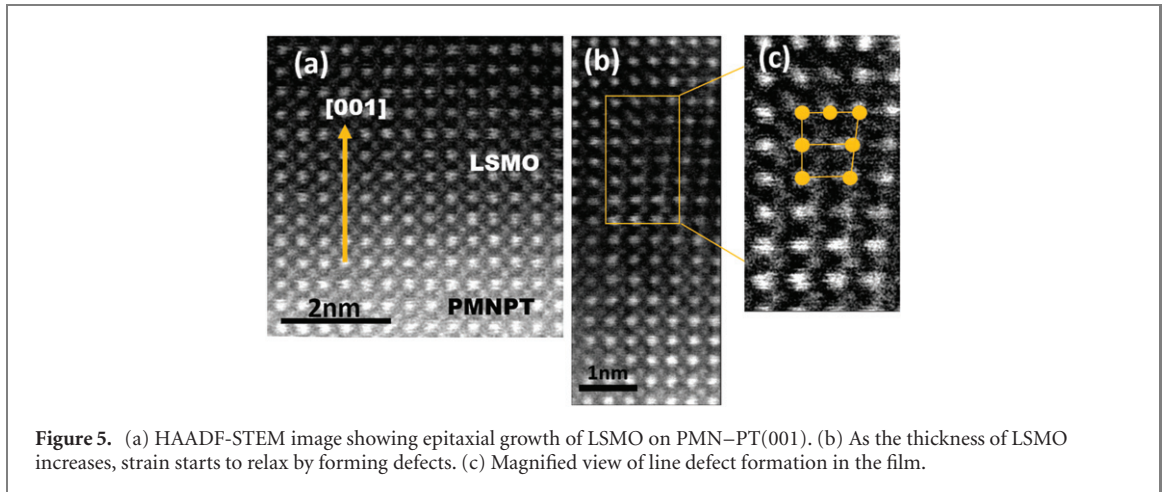
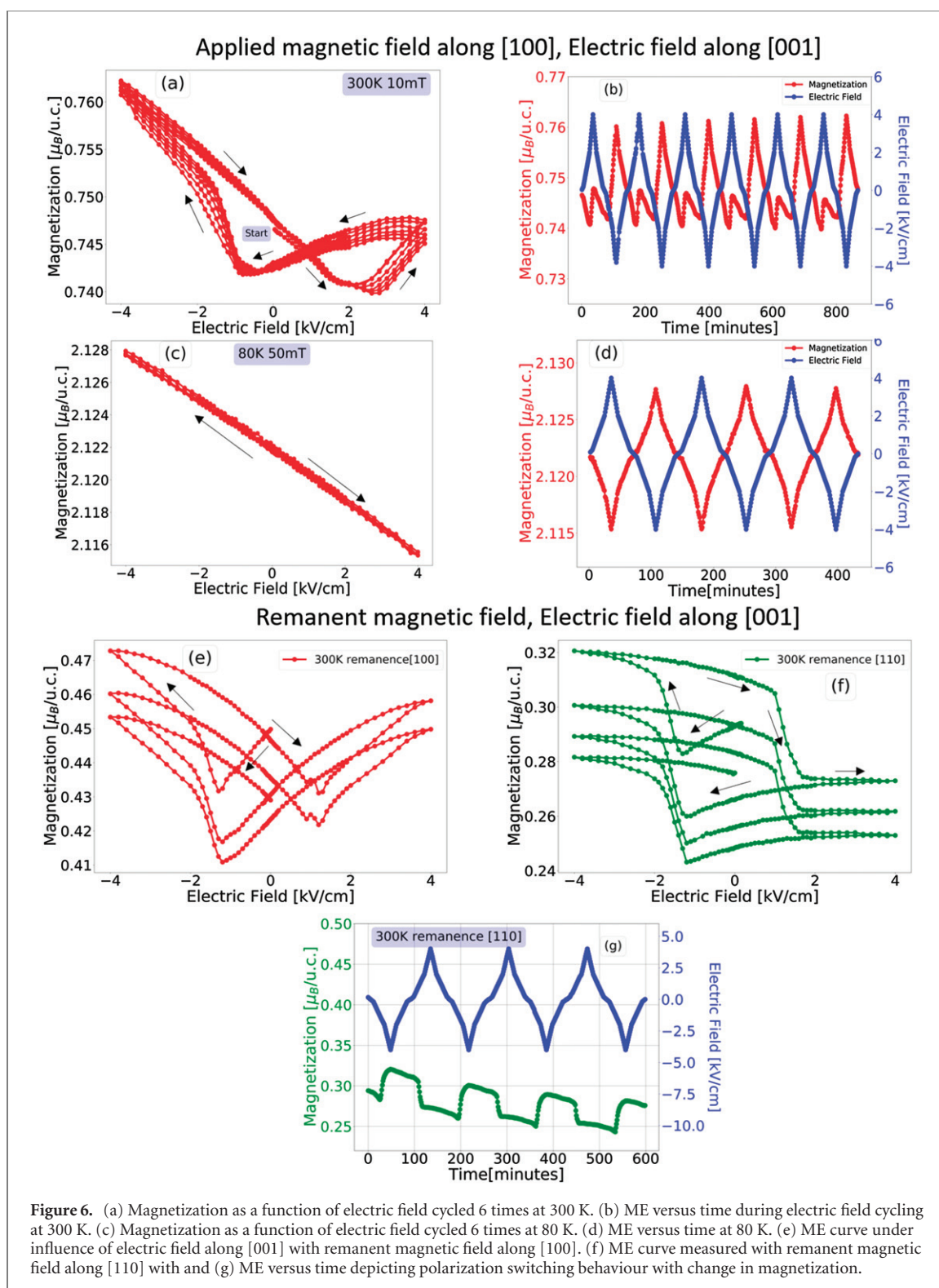


Figure 5. (a) HAADF-STEM image showing epitaxial growth of LSMO on PMN-PT(001). (b) As the thickness of LSMO increases, strain starts to relax by forming defects. (c) Magnified view of line defect formation in the film.

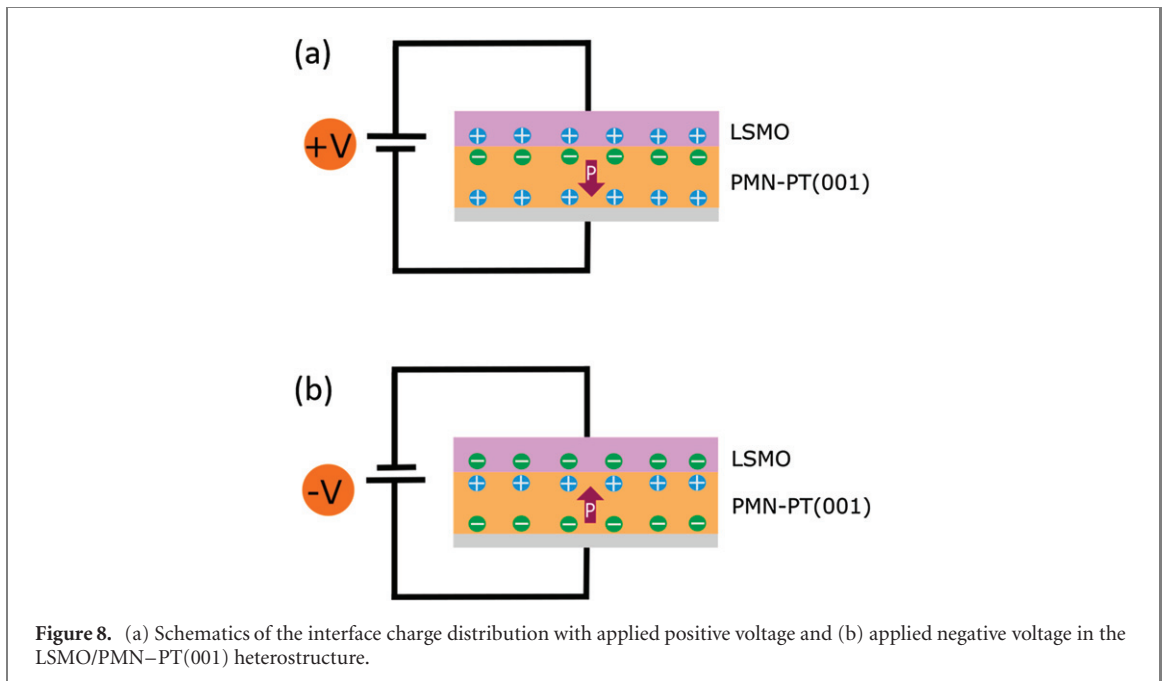
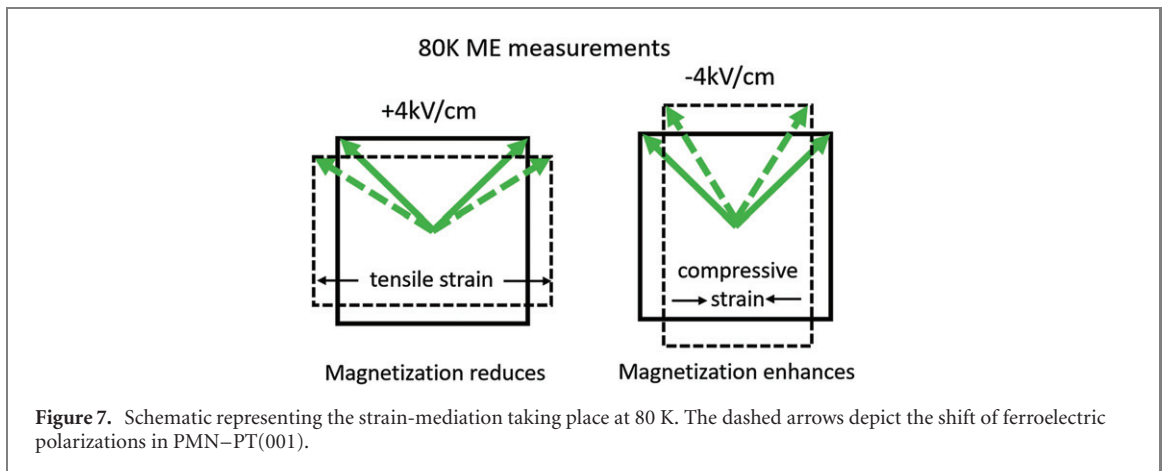
in-plane tensile strain, it tends to favour in-plane orbital occupancy resulting in the in-plane easy axis [5]. LSMO film grown on PMN-PT(001) has easy axis along the face diagonals $[110]$ and $[1\bar{1}0]$ and the hard axis is along $[100]$. The first set of measurements are recorded at two temperatures and two magnetic fields: 300 K, 10 mT and 80 K, 50 mT. The magnetic field is applied along $[100]$ and the electric field is applied along $[001]$. With the applied magnetic field of 10 mT (300 K) and 50 mT (80 K), the magnetization in LSMO/PMN-PT is near saturation, but not saturated and therefore, the influence of both magnetic and electric field can be observed.

The electric field loops follow $0 \text{ kV cm}^{-1} \rightarrow +4 \text{ kV cm}^{-1} \rightarrow 0 \text{ kV cm}^{-1} \rightarrow -4 \text{ kV cm}^{-1} \rightarrow 0 \text{ kV cm}^{-1}$. In these measurements, the magnetic moments of LSMO follow the magnetic field as well as the electric field i.e., there are two forces acting playing a role in this ME measurements. Therefore, the results obtained are function of both, applied magnetic field as well as applied electric field. Figures 6(a) and (b) depicts a butterfly loop characteristic of strain-mediated ME coupling [9] and correlation with time at 300 K with 10 mT. However, the presence of asymmetry in butterfly loop with the cross-over point around $+1 \text{ kV cm}^{-1}$ indicates the presence of another effect contributing to it as a pure strain-mediated coupling would have a symmetric butterfly loop. The difference between the magnetization obtained at $+4 \text{ kV cm}^{-1}$ and -4 kV cm^{-1} is about 2%. The second set of measurements is performed at 80 K with 50 mT which shows a different ME behaviour compared to the one observed at 300 K. At such low temperature the piezoelectric strains in PMN-PT are severely reduced leading to hardening of ‘polarization rotation’ [25], which results in change of strain behaviour from butterfly to linear as shown in figures 6(c) and (d). For our measurements at 80 K, the polarization is already poled with negative bias of voltage from the last voltage loop at 300 K in the sample. The sample is then cooled to 80 K with applied magnetic field of 50 mT. When -4 kV cm^{-1} is applied, the polarization pointing upwards tends to align along the electric field as shown in figure 7 resulting in compressive strain, thereby enhancing the magnetization. On applying $+4 \text{ kV cm}^{-1}$, the polarization tries to switch and follow the electric field, but due to polarization hardening it is unable to rotate resulting in the tensile strain. Effectively this amount of electric field cannot switch the polarization state from up to down and only results in a slight tilting of the polarization vector causing a linear strain change. The electric coercive field of PMN-PT increases with decreasing temperature which is why the ferroelectric polarization is not possible with such small amount of applied electric field. Therefore, the ME coupling at 80 K is a strain-mediated coupling effect. The magnetization is normalized to $\mu_B/\text{u.c.}$ by measuring the deposited area and the thickness of the film, leading to a systematic error of about 4% for the absolute value of the magnetization. The statistical error is several orders of magnitude smaller than the magnetization value.

To investigate the pure influence of electric field, measurements are performed in remanent magnetic field: for 300 K 10 mT is applied and removed and for 80 K, 50 mT is used and the ME behaviour is recorded along easy axis $[110]$ and hard axis $[100]$ for LSMO. For 80 K measurements, we observe no significant change along either direction; linear strain behaviour is observed. However, at 300 K in remanent magnetic field, the nature of ME coupling changes from prominently strain-mediated along $[100]$, figure 6(e) to hysteresis loop like behaviour along $[110]$, figure 6(f). This hysteresis loop like behaviour shows the presence of ferroelectric polarization switching effect. Plotting it against time, figure 6(g), one can see the switching behaviour of magnetization is evident at the coercive field (E_c) of PMN-PT around $\pm 1.5 \text{ kV cm}^{-1}$. In remanent magnetic field, the magnetic moments are no longer affected by magnetic field and are free to follow the electric field only. Thus, near E_c , the switching of polarization occurs resulting in



change in magnetization of LSMO based on charge-mediated ME coupling. As the PMN–PT substrate is both piezoelectric and ferroelectric, both effects contribute to the ME coupling. Based on the influencing parameters, the nature of ME coupling is significantly affected at the room temperature. The strain-mediated ME coupling is stronger along hard axis of LSMO whereas the charge mediated ME coupling has prominence along the easy axis of LSMO. We take this as an evidence of contribution from charge coupling, alongside the strain coupling, in LSMO/PMN–PT(001) along the hard axis [100] and dominance of ferroelectric switching effect along the easy axis [110]. The asymmetric butterfly loop (figure 6(a)) arises due to contribution from both strain and charge-mediated ME coupling as a purely strain coupled system exhibits a symmetric butterfly loop. However, the presence of ferroelectricity in PMN–PT makes charge mediated coupling plausible.



For the charge-mediated coupling taking place at the interface of LSMO/PMN–PT(001), one has to take into account the polarization directions in PMN–PT(001). With eight possible polarization directions along $\langle 111 \rangle$, the polarization rotates towards $[00\bar{1}]$ direction on applying positive voltage and towards $[001]$ direction for negative voltage [26]. This gives rise to charge accumulation in LSMO. On applying a positive voltage to LSMO, positive charges are accumulated whereas for a negative voltage, negative charges are accumulated in LSMO as shown in figure 8. This accumulation of charges affect the $\text{Mn}^{3+}/\text{Mn}^{4+}$ ratio close to the interface which is responsible for the double exchange interaction in LSMO. The accumulation of negative charges in LSMO causes a reduction in Mn^{4+} ions which can further strengthen the double exchange interaction in LSMO, whereas the accumulation of positive charges in LSMO weakens the double exchange interaction [27, 28]. Therefore, a higher magnetization is obtained for $-V$ and lower magnetization is obtained for $+V$, as can be seen clearly in figure 6(b). The accumulation of charges along with the redistribution of oxygen vacancies in LSMO due to ferroelectric switching, together contribute to the interfacial charge coupling in LSMO/PMN–PT(001).

Upon removing the voltage, the polarizations does not switch back to its initial state due to ferroelectric effect and a certain amount of electric field is required to switch the polarizations. Thus, the accumulation of positive and negative charges at LSMO/PMN–PT interface continues giving rise to a change in magnetization. The results so far indicate that the strain part is responsible for the volatile coupling causing the butterfly loop and the ferroelectric effect governs the non-volatile coupling leading to a remanent change in magnetization.

In hysteresis loops, a change in coercive field, H_C , is observed upon removing the voltage from the sample. Figure 9 depicts magnetization versus applied magnetic field curves measured at different

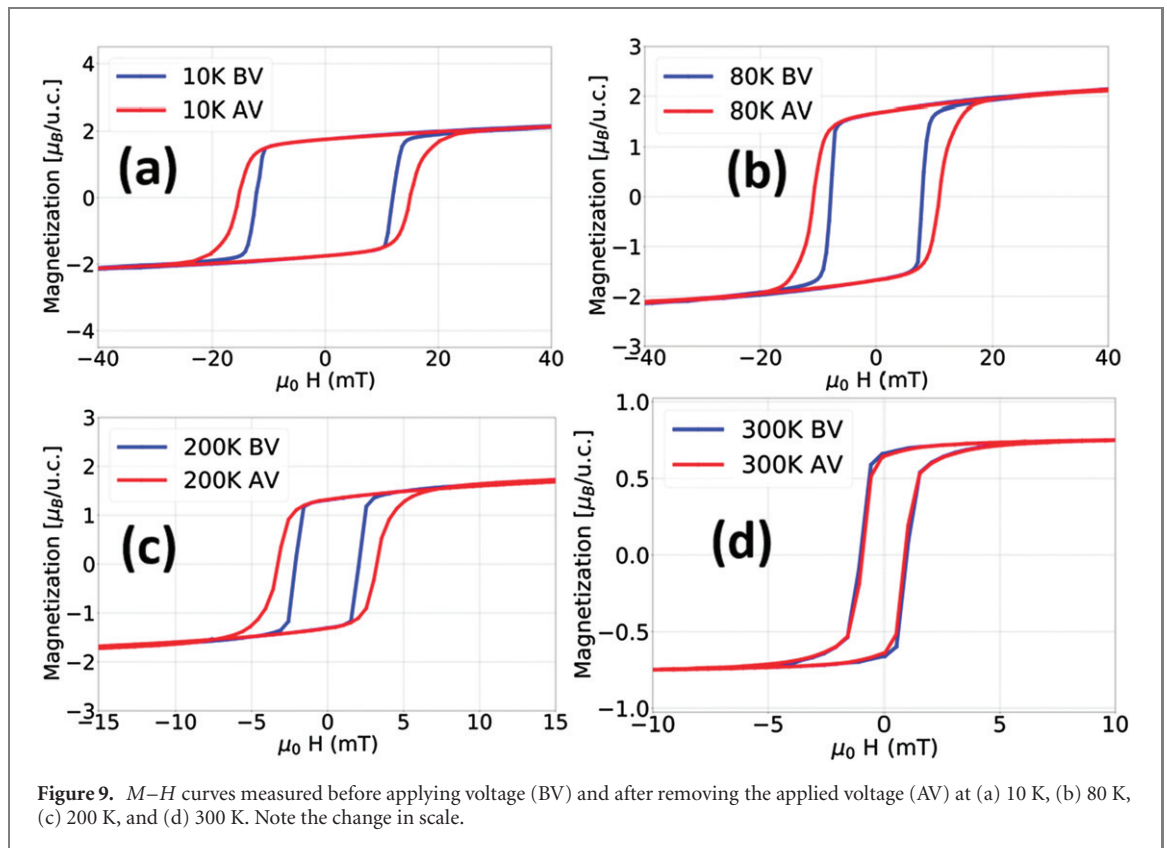


Figure 9. M - H curves measured before applying voltage (BV) and after removing the applied voltage (AV) at (a) 10 K, (b) 80 K, (c) 200 K, and (d) 300 K. Note the change in scale.

Table 1. H_C before application of voltage (BV), after removal of voltage (AV), and percentage change. Uncertainty in H_C is ± 0.1 mT.

T (K)	H_C BV (mT)	H_C AV (mT)	Change (%)
10	12.1	15.1	+25%
80	7.8	10.7	+37%
200	2.1	3.3	+62%
300	-0.9	-0.9	Within error

temperatures: 10 K, 80 K, 200 K and 300 K. The after voltage measurements are performed after the sample has seen six voltage cycles. At low temperatures (10 K, 80 K, 200 K), there is an increase in H_C after the voltage is removed. However, at 300 K no change can be observed within the error in H_C after voltage removal. It is known that coercivity is directly related to magnetic anisotropy energy and magnetic anisotropy energy increases along the hard axis and decreases along the easy axis. Also, magnetic anisotropy energy increases under tensile strain [29]. We have seen from the ME measurements above that the system is still under remanent strain even after removing the voltage which is due to the contribution from charge-mediated ME coupling. Therefore, when the electric field is turned off, due to the presence of this remanent tensile strain in the system, it leads to higher magnetic anisotropy energy and higher coercivity along the hard axis [100] of LSMO. The magnetic anisotropy energy is dominant at low temperatures and that is why the change in H_C is significant at low temperatures [30, 31] whereas at 300 K the anisotropy field is mostly dependent on shape anisotropy, thus, the change is not significant. Table 1 lists the change in coercive field at different temperatures. The highest relative increase in H_C is observed at 200 K.

3.3. Polarized neutron reflectometry

The magnetic depth profile of LSMO/PMN-PT(001) is probed via PNR depicted in figure 10. The measurement is performed at 80 K with applied magnetic field of 50 mT at different electric field steps: 0 kV cm^{-1} , -4 kV cm^{-1} and $+4 \text{ kV cm}^{-1}$. The PNR curves corresponding to $+4 \text{ kV cm}^{-1}$ are depicted in supplementary material figure S1 (<https://stacks.iop.org/NJP/23/063043/mmedia>). The reflectivity data were model fit using Refl1D [32], which uses a matrix transfer algorithm to calculate the reflectivity from a one-dimensional scattering length density profile. On applying voltage to the sample discussed in this work, the surface corrugates, leading to deviations from this 1D limit (scattered beam broadening) [33]. While a 2D analysis might strictly provide a fuller and more accurate accounting of the broadening of the reflection,

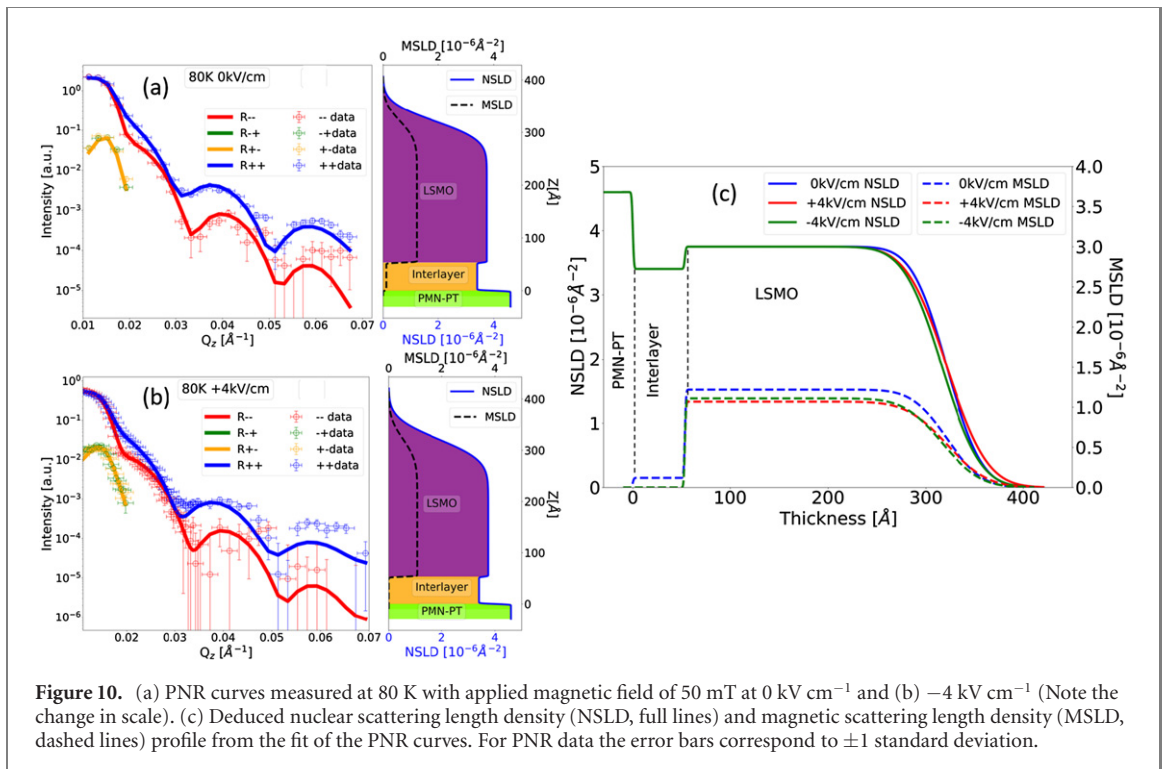
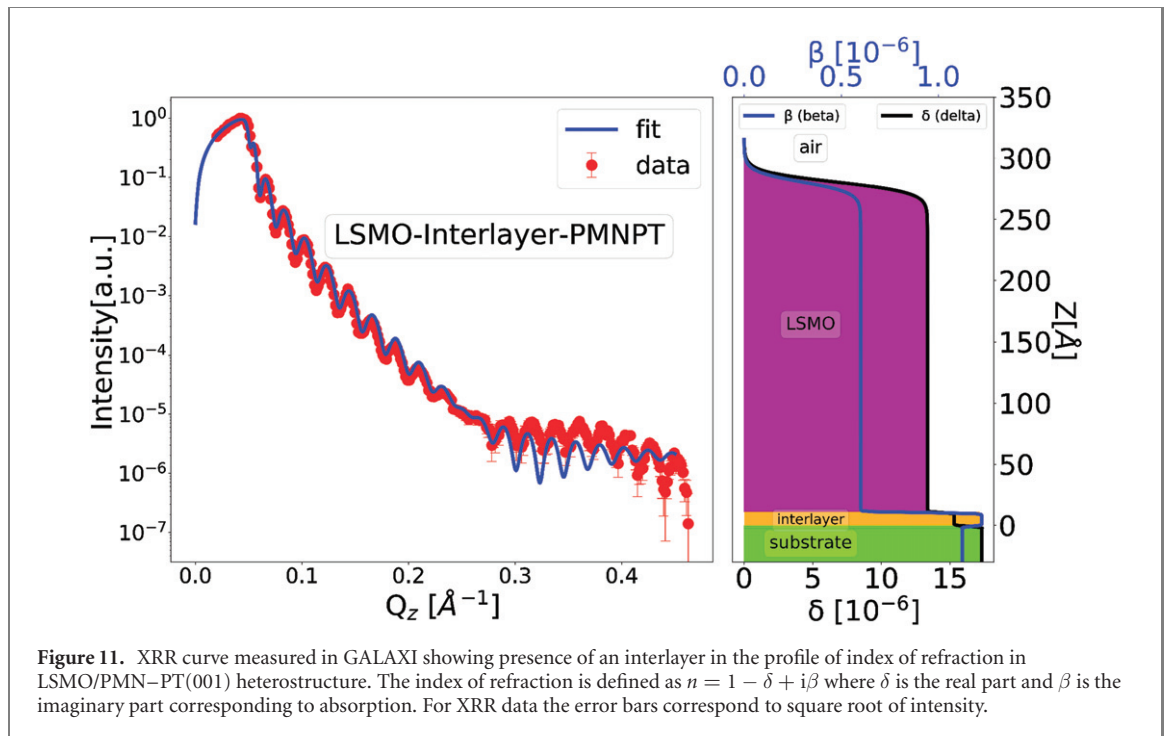


Figure 10. (a) PNR curves measured at 80 K with applied magnetic field of 50 mT at 0 kV cm⁻¹ and (b) -4 kV cm⁻¹ (Note the change in scale). (c) Deduced nuclear scattering length density (NSLD, full lines) and magnetic scattering length density (MSLD, dashed lines) profile from the fit of the PNR curves. For PNR data the error bars correspond to ± 1 standard deviation.

and some related artefacts are evident in our model fits, the sample and the associated scattering is still close enough to the 1D limit for the purposes of the conclusions drawn in this work [34]. The spin-flip signal in the plots is shown until 0.02 \AA^{-1} as the intensity becomes zero within the error bars. The physical model used for this system comprises of an LSMO layer with constant magnetic scattering length density (MSLD) along with interlayer, for which the nuclear scattering length density (NSLD) and MSLD are allowed to vary between the values for the substrate and the film. The top interface of the film is not very smooth due to some ageing effect. Scattering length density (SLD) is a measure of scattering from the scattering cross-section of a material and their scattering length depends on the strength of interaction between the neutrons and a given nucleus. MSLD accounts for the magnetization of the probed sample and NSLD gives information about stoichiometric fluctuations, film roughness and substrate roughness.

Figure 10(c) depicts the depth profile of LSMO/PMN-PT(001) at different electric fields. The deduced model from the fit of PNR curves shows an LSMO layer thickness of $268^{+2}_{-1} \text{ \AA}$ and the presence of an 53^{+1}_{-1} \AA thick interlayer with reduced nuclear (NSLD) and magnetic (MSLD) scattering length densities. The spin-flip signal resulting from the angle of magnetization in LSMO is due to non-saturated LSMO film and the fitting model uses angle of about $\sim 18^\circ$ from the quantization axis of the polarized neutron beam. Though the angle of magnetization remains constant throughout the depth of film. The observed magnetization for LSMO and the interlayer is highest for 0 kV cm⁻¹ and drops for the other electric fields. This is due to change in the sample quality which is evident from the broadening of reflected beam. Also, one has to mention that the starting state of the magnetization for the PNR samples and SQUID is different. In SQUID measurements, the sample first cycles through six voltage loops at 300 K and then it is cooled to 80 K for the next set of voltage loops. The drop in magnetization has been observed in the first voltage cycle for initial voltage steps before the magnetization starts following the loop. Therefore, when 0 kV cm⁻¹ is measured at 80 K in SQUID, the magnetization has already been reduced whereas for PNR measurements, the magnetization for 80 K at 0 kV cm⁻¹ is recorded in the virgin state of sample. This is the reason of observing higher magnetization at 80 K for 0 kV cm⁻¹ and the drop in magnetization from ungated to gated case in PNR. Since, the PNR measures vector magnetization of the sample and the SQUID measures the longitudinal component of the magnetization, therefore from the relation: $M_L = M \cos \theta$, (taking $\theta = 18^\circ$, M_L = longitudinal component of magnetization and M = vector magnetization), we get the magnetization M_L for gated cases from PNR: $M_L(-4 \text{ kV cm}^{-1}) = 2.31 \pm 0.06 \mu_B/\text{u.c.}$ and $M_L(+4 \text{ kV cm}^{-1}) = 2.22 \pm 0.08 \mu_B/\text{u.c.}$ and from SQUID: $M_L(-4 \text{ kV cm}^{-1}) = 2.13 \mu_B/\text{u.c.}$ and $M_L(+4 \text{ kV cm}^{-1}) = 2.11 \mu_B/\text{u.c.}$. Therefore, the effect of strain-mediated ME coupling is visible from both PNR and SQUID. Confidence interval for the errors of PNR fit is 95%. The reduced NSLD and MSLD at interlayer reflects towards a plausible stoichiometric fluctuation at the interface which is further studied using TEM.



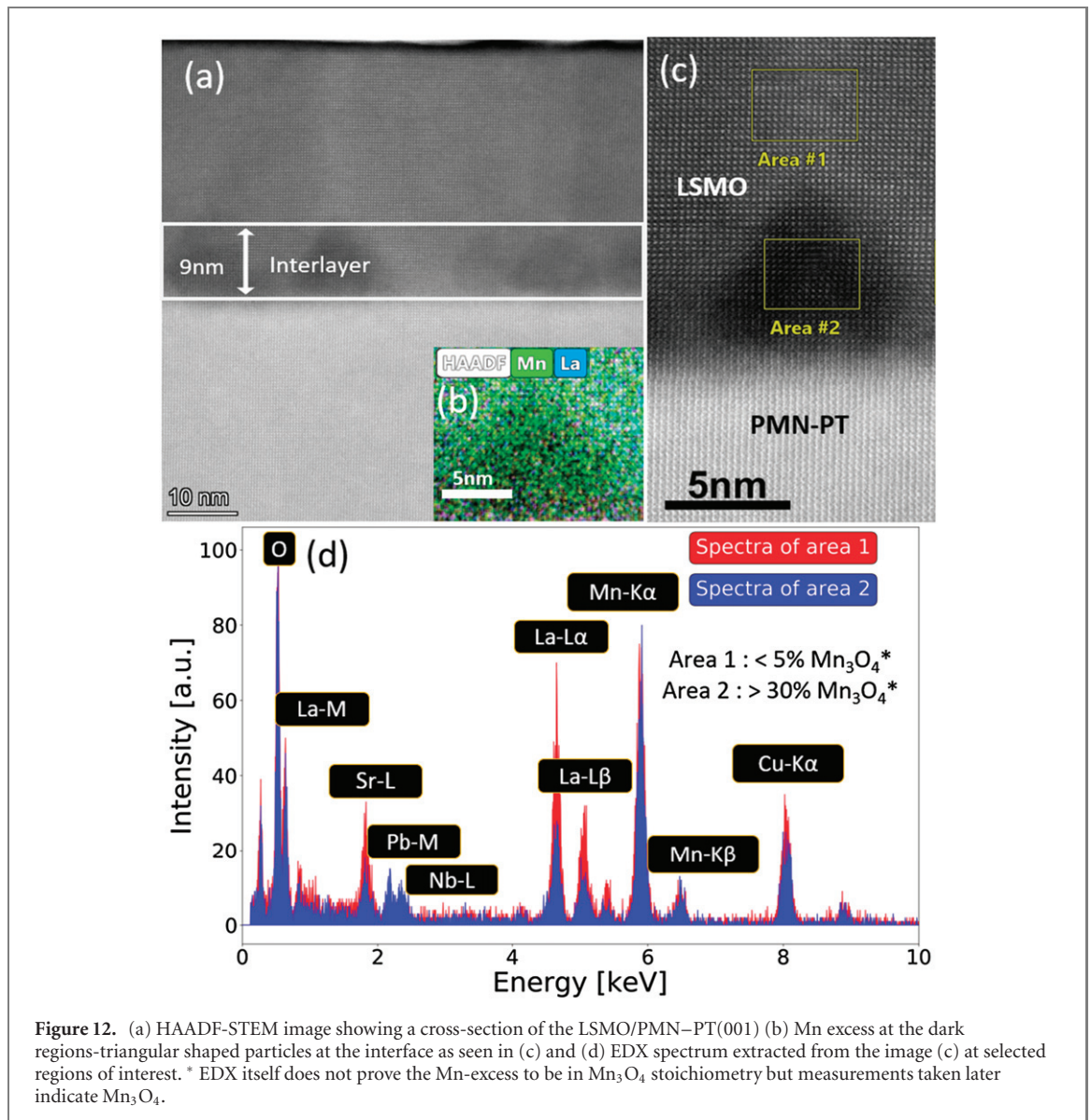
3.4. X-ray reflectivity

A similar sample is measured using x-rays with our in-house instrument GALAXI (gallium anode low-angle x-ray instrument) [35] to determine the thickness. Figure 11 demonstrates the dampening of oscillations between Q_z of 0.2–0.3 \AA^{-1} which is due to the intrinsic formation of the interlayer in the system. The deduced thickness of the LSMO and interlayer from the XRR plot is $270 \pm 1 \text{ \AA}$ and $11 \pm 3 \text{ \AA}$ respectively. The interlayer thickness obtained from PNR and XRR are different as the formation of interlayer is an intrinsic property of the heterostructure depending on the growth conditions and can vary from sample to sample. In supplementary material, figure S2 shows a fitting model for XRR in which only LSMO on PMN-PT has been taken into account and one can clearly see from the fit that the inclusion of the interlayer is crucial to get a good fit for this system. The fitting for XRR data is performed using BornAgain [36].

3.5. TEM analysis

To get more insight on the interlayer, TEM measurements are performed. From figure 12(a) one can see the presence of dark regions at the interface. Elemental mapping identifies the stoichiometric fluctuation as manganese excess (insets in figures 12(b) and (c)). With energy-dispersive x-ray (EDX) analysis, we are able to deduce that area 1 has less than 5% Mn_3O_4 and in the dark particle region area 2 has more than 30% of Mn_3O_4 concentration. There is slight inter-diffusion of Pb and Nb near the interface as observed in EDX spectra. Evidence of these Mn_3O_4 is visible in zero-field cooling (ZFC) and field cooling curves (FCC) measured with applied field of 50 mT shown in figure 13. It has to be noted that the size of Mn_3O_4 particles can vary from sample to sample as its an intrinsic formation during growth. The height of these triangular Mn_3O_4 particles is about 80–90 \AA in the sample used for TEM.

The kink in the magnetization around 43 K, which is the Curie temperature of Mn_3O_4 , hints to the particle stoichiometry to be Mn_3O_4 [37]. This fits well with the PNR model which shows drop of NSLD at the interlayer as Mn has a negative scattering length. The formation of Mn_3O_4 particles at the interlayer is not surprising due to its chemical compatibility with the whole manganite perovskite family [38]. Mn_3O_4 crystallizes in a distorted spinel structure with tetrahedral A-sites occupied by Mn^{2+} ion and the octahedral B-sites are occupied by Mn^{3+} ions [39, 40] with cell parameters of $a = 5.76 \text{ \AA}$ and $c = 9.47 \text{ \AA}$. The manganese segregation in such a compound usually occurs due to La-deficiency which is visible in figure 12 and the appearance of manganese oxide at the interface appears in a stochastic manner as seen from TEM images. The biaxial in-plane compressive strain from PMN-PT(001) and high oxygen partial pressure during growth allows Mn_3O_4 to grow epitaxially in cubic phase [41–43]. When growing on PMN-PT(001), Mn_3O_4 experiences in-plane compressive strain of -1.2% which is smaller compared to $+3.5\%$ in-plane tensile strain experienced by LSMO, thus making it energetically favourable for Mn_3O_4 to nucleate on top of the substrate. TEM images show the possible presence of triangular shaped- Mn_3O_4 particles at the



interlayer. For the sample used for PNR measurements, it was calculated based on the drop of NSLD, that the interlayer is composed of about 15% Mn_3O_4 particles and 85% of LSMO. The Mn_3O_4 particles therefore represent approximately 2%–3% of the overall film volume, including both interlayer and bulk.

3.6. Negative remanence

Interestingly, an inverted hysteresis loop with negative remanence is observed for 300 K whereas for other temperatures, the magnetization follows the normal hysteresis loop (NHL) shown in figure 14. We observe that at $T = 270$ K (figure S3, supplementary material), with H in positive direction, the M_r is negative. The appearance of negative remanence means that the direction of magnetization is reversed to the direction of applied magnetic field. This indicates that there is probably some other magnetic ordering present in the system which is able to switch the magnetization of LSMO at this temperature. The initial speculation is based on the results reported by Mottaghi *et al* [44] and Kumari *et al* [45] where they observed negative remanence due to the presence of magnetically inhomogeneous spin cluster regions. In our system, we observe Mn_3O_4 particles at the interface which are ferrimagnetic with $T_c = 43$ K [37], but are paramagnetic at 270 K where we observe negative remanence effect, therefore they cannot influence the magnetization of LSMO at higher temperatures. However, we also observe reduced magnetization at the interlayer as seen from PNR measurements which is due to presence of Mn_3O_4 particles, defects near the interface as shown in figure 5, as well as the strong in-plane tensile strain imparted on LSMO deposited on PMNPT. The magnetic behaviour of LSMO is governed by the double exchange interaction between $\text{Mn}^{3+}-\text{O}^{2-}-\text{Mn}^{4+}$ bond. Now, if there is presence of defects or/oxygen vacancies in the film, it can break this exchange interaction resulting in higher spin disorder [45]. In addition, it is well known that tensile strain can

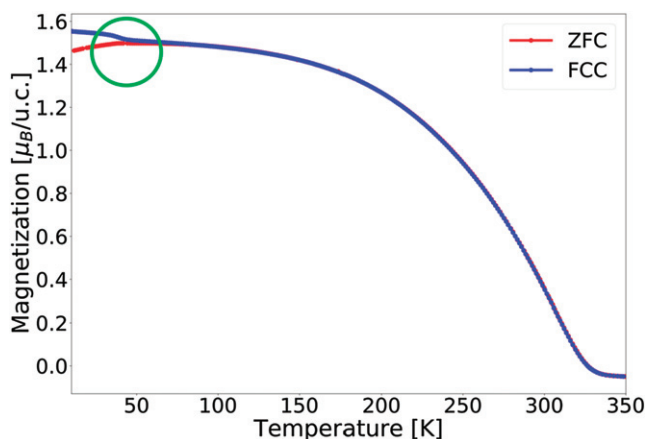


Figure 13. ZFC and FCC curve showing a kink in magnetization around 43 K, the Curie temperature of Mn_3O_4 .

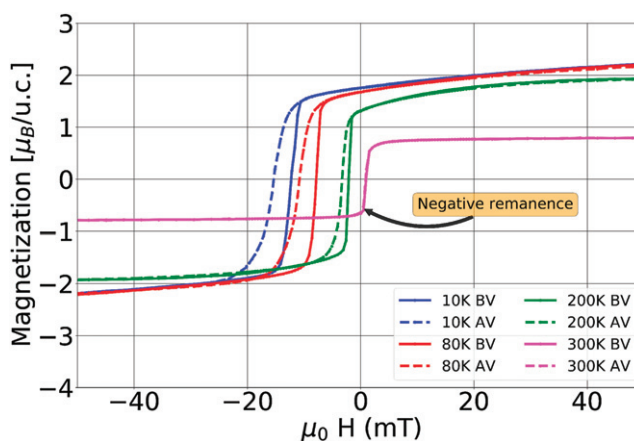


Figure 14. First half (applied magnetic field goes from $+2.5$ T to -2.5 T) of the hysteresis loops from figure 9 to show the negative remanence at 300 K.

suppress the ferromagnetism in LSMO due to strain-induced distortions of MnO_6 octahedra. From the above results one can see that there are structural inhomogeneities consisting of spin clusters localized at the interface [17, 46, 47]. At higher temperature, the spin disorder is high due to thermal energy and with the presence of magnetically inhomogeneous spin cluster regions, it may become plausible to switch the magnetization direction in LSMO. Further systematic measurements are needed to understand this behaviour.

4. Summary and conclusion

In conclusion, we report the growth of LSMO thin film on PMN-PT(001) with good crystalline quality. The magnetic properties of the sample shows a stable ferromagnetic state of LSMO. The influence of different parameters has been demonstrated: change of strain behaviour from butterfly to linear as a function of temperature, dominance of strain-coupling along hard axis [100] of LSMO and ferroelectric polarization effect leading to charge-coupling along easy axis [110] of LSMO in remanent magnetic field. The observed change in H_C as a function of temperature after removing the applied voltage arises due to the magnetic anisotropy energy. In addition, negative remanence is observed for 300 K whereas other temperatures showed NHLs. With first speculations, the appearance of negative remanence effect has been attributed to the inhomogeneous spin cluster regions near the interface but further systematic study is required to clearly understand this behaviour. The magnetic depth profile is studied using PNR which shows the presence of an interlayer with stoichiometric fluctuation causing a drop in the NSLD of the interlayer. This interlayer is found to have reduced magnetization compared to bulk of the film, which is not very surprising owing to the fact that high tensile strain can suppress ferromagnetism in LSMO. However, studying the interface of LSMO and PMN-PT by TEM, reveals the presence of Mn_3O_4 particles which are

also visible in ZFC and FCC curves by the kink in the magnetization at 43 K. Due to a good chemical compatibility, Mn_3O_4 can grow easily in an LSMO matrix. From these results a comprehensive understanding of ME coupling in LSMO/PMN-PT(001) as a function of temperature and directional dependence is obtained.

Acknowledgments

The authors thank Oleg Petravic for fruitful discussions regarding magnetometry and the magnetoelectric set-up. The authors would also like to thank Lidia Kibkalo for FIB sample preparation, Berthold Schmitz and Frank Gossen for technical support.

Data availability statement

The data that support the findings of this study are available upon reasonable request from the authors.

ORCID iDs

T Bhatnagar-Schöffmann  <https://orcid.org/0000-0003-2662-122X>

E Kentzinger  <https://orcid.org/0000-0002-5348-7591>

A Sarkar  <https://orcid.org/0000-0002-2744-0378>

P Schöffmann  <https://orcid.org/0000-0002-6393-7090>

Q Lan  <https://orcid.org/0000-0002-9215-4925>

L Jin  <https://orcid.org/0000-0001-6924-2364>

A Kovács  <https://orcid.org/0000-0001-8485-991X>

A J Grutter  <https://orcid.org/0000-0002-6876-7625>

B J Kirby  <https://orcid.org/0000-0003-2472-3791>

R Beerwerth  <https://orcid.org/0000-0001-5100-4229>

A Stellhorn  <https://orcid.org/0000-0003-2868-657X>

U Rücker  <https://orcid.org/0000-0002-0200-6989>

R E Dunin-Borkowski  <https://orcid.org/0000-0001-8082-0647>

Th Brückel  <https://orcid.org/0000-0003-1378-0416>

References

- [1] Maniaturuni S *et al* 2019 *Nature* **565** 35–42
- [2] Sahoo S, Polisetty S, Duan C G, Jaswal S S, Tsymlal E Y and Binek C 2007 *Phys. Rev. B* **76** 092108
- [3] Duan C-G, Velev J P, Sabirianov R F, Mei W N, Jaswal S S and Tsymlal E Y 2008 *Appl. Phys. Lett.* **92** 122905
- [4] Borisov P, Hochstrat A, Chen X, Kleemann W and Binek C 2005 *Phys. Rev. Lett.* **94** 117203
- [5] Song C, Cui B, Li F, Zhou X and Pan F 2017 *Prog. Mater. Sci.* **87** 33–82
- [6] Schmitz M, Weber A, Petravic O, Waschk M, Zakalek P, Mattauch S, Koutsiousbas A and Brückel T 2020 *New J. Phys.* **22** 053018
- [7] Chu Y-H *et al* 2008 *Nat. Mater.* **7** 478–82
- [8] Molegraaf H J A, Hoffman J, Vaz C A F, Gariglio S, van der Marel D, Ahn C H and Triscone J-M 2009 *Adv. Mater.* **21** 3470–4
- [9] Thiele C, Dörr K, Bilani O, Rödel J and Schultz L 2007 *Phys. Rev. B* **75** 054408
- [10] Pati S P and Taniyama T 2019 *J. Phys. D: Appl. Phys.* **53** 054003
- [11] Vaz C A F, Hoffman J, Ahn C H and Ramesh R 2010 *Adv. Mater.* **22** 2900–18
- [12] Hemberger J, Krimmel A, Kurz T, Krug von Nidda H A, Ivanov V Y, Mukhin A A, Balbashov A M and Loidl A 2002 *Phys. Rev. B* **66** 094410
- [13] Haghiri-Gosnet A-M and Renard J-P 2003 *J. Phys. D: Appl. Phys.* **36** R127–50
- [14] Momma K and Izumi F 2011 *J. Appl. Crystallogr.* **44** 1272–6
- [15] Zhang S and Li F 2012 *J. Appl. Phys.* **111** 031301
- [16] Ho J C, Liu K S and Lin I N 1993 *J. Mater. Sci.* **28** 4497–502
- [17] Huijben M, Martin L W, Chu Y H, Holcomb M B, Yu P, Rijnders G, Blank D H A and Ramesh R 2008 *Phys. Rev. B* **78** 094413
- [18] Vailionis A, Boschker H, Siemons W, Houwman E P, Blank D H A, Rijnders G and Koster G 2011 *Phys. Rev. B* **83** 064101
- [19] Waschk M 2017 Interface phenomena in $\text{La}_{1/3}\text{Sr}_{2/3}\text{FeO}_3/\text{La}_{2/3}\text{Sr}_{1/3}\text{MnO}_3$ heterostructures and a quest for p-electron magnetism *PhD Thesis RWTH Aachen University*
- [20] Ernst Ruska-Centre for Microscopy and Spectroscopy with Electrons (ER-C) *et al* 2016 FEI Titan G2 80-200 CREWLEY J. *Large-Scale Res. Facil.* **2** A43
- [21] Murr L E 2015 *Line Defects: Dislocations in Crystalline Materials* (Berlin: Springer) pp 235–71
- [22] Borisov P, Hochstrat A, Shvartsman V V and Kleemann W 2007 *Rev. Sci. Instrum.* **78** 106105
- [23] Wang L-M, Petravic O, Kentzinger E, Rücker U, Schmitz M, Wei X-K, Heggen M and Brückel T 2017 *Nanoscale* **9** 12957–62
- [24] Wang L-M, Petravic O, Mattauch S, Koutsiousbas A, Wei X-K, Heggen M, Leffler V, Ehler S and Brückel T 2018 *J. Phys. D: Appl. Phys.* **52** 065301
- [25] Li F, Zhang S, Xu Z, Wei X, Luo J and Shrout T R 2010 *Appl. Phys. Lett.* **96** 192903
- [26] Wang P, Jin C, Wang Y C, Liu S S, Wang X Y, Zheng D X, Zheng W C and Bai H L 2020 *J. Appl. Phys.* **127** 244102

- [27] Li D, Zheng D, Gong J, Zheng W, Jin C and Bai H 2017 *ACS Appl. Mater. Interfaces* **9** 24331–8
- [28] Vaz C A F, Hoffman J, Segal Y, Reiner J W, Grober R D, Zhang Z, Ahn C H and Walker F J 2010 *Phys. Rev. Lett.* **104** 127202
- [29] Guo Q *et al* 2018 *Nanotechnology* **29** 224003
- [30] Steenbeck K and Hiergeist R 1999 *Appl. Phys. Lett.* **75** 1778–80
- [31] Chaluvadi S K *et al* 2018 *Appl. Phys. Lett.* **113** 052403
- [32] Kirby B J, Kienzle P A, Maranville B B, Berk N F, Krycka J, Heinrich F and Majkrzak C F 2012 *Curr. Opin. Colloid Interface Sci.* **17** 44–53
- [33] Jamer M E *et al* 2018 *Phys. Rev. Appl.* **10** 044045
- [34] Majkrzak C, O'Donovan K and Berk N 2005 *Neutron Scattering from Magnetic Materials (Polarized Neutron Reflectometry)* (Amsterdam: Elsevier) pp 397–471
- [35] Jülich Centre for Neutron Science 2016 *J. Large-Scale Res. Facil.* **2** A61
- [36] Pospelov G, Van Herck W, Burle J, Carmona Loaiza J M, Durniak C, Fisher J M, Ganeva M, Yurov D and Wuttke J 2020 *J. Appl. Crystallogr.* **53** 262–76
- [37] Boucher B, Buhl R and Perrin M 1971 *J. Appl. Phys.* **42** 1615–7
- [38] Mukherjee D, Bingham N, Hordagoda M, Phan M-H, Srikanth H, Witanachchi S and Mukherjee P 2012 *J. Appl. Phys.* **112** 083910
- [39] Pattanayak J, Sitakara Rao V and Maiti H S 1989 *J. Mater. Sci. Lett.* **8** 1405–7
- [40] Suzuki T and Katsufuji T 2008 *Phys. Rev. B* **77** 220402
- [41] Bi Z, Weal E, Luo H, Chen A, MacManus-Driscoll J L, Jia Q and Wang H 2011 *J. Appl. Phys.* **109** 054302
- [42] Pomar A *et al* 2016 *Front. Phys.* **4** 41
- [43] Jian H, Zhang Z, Wang Y, Tang X, Yang J, Hu L, Chen L, Zhu X and Sun Y 2013 *J. Alloys Compd.* **561** 95–100
- [44] Mottaghi N *et al* 2018 *J. Phys.: Condens. Matter.* **30** 405804
- [45] Kumari S, Mottaghi N, Huang C-Y, Trappen R, Bhandari G, Yousefi S, Cabrera G, Seehra M S and Holcomb M B 2020 *Sci. Rep.* **10** 3659
- [46] Moon E J *et al* 2014 *Nano Lett.* **14** 2509–14
- [47] Tebano A *et al* 2008 *Phys. Rev. Lett.* **100** 137401